Erschienen in: Advanced Materials Interfaces ; 4 (2017), 1. - 1600431
https://dx.doi.org/10.1002/admi.201600431

Self-Assembled Magnetite Mesocrystalline Films: Toward Structural Evolution from 2D to 3D Superlattices

J. Brunner, I. A. Baburin, S. Sturm, K. Kvashnina, A. Rossberg, T. Pietsch, S. Andreev, E. Sturm (née Rosseeva), and H. Cölfen**

This study describes synthesis and detailed characterization of 2D and 3D mesocrystalline films produced by self-assembly of iron oxide (magnetite) truncated nanocubes. The orientational relations between nanocrystals within the superlattice are examined and atomistic models are introduced. In the 2D case, two distinct superstructures (i.e., translational order) of magnetite nanocubes can be observed with *p4mm* and *c2mm* layer symmetries while maintaining the same orientational order (with $[100]_{magnetite}$ perpendicular to the substrate). The 3D structure can be approximated by a slightly distorted face-centered cubic (fcc) superlattice. The most efficient space filling within the 3D superstructure is achieved by changing the orientational order of the nanoparticles and following the "bump-to-hollow" packing principle. Namely orientational order is determined by the shape of the nanoparticles with the following orientational relations: $[001]_{SL}||[310]_{magnetite}$, $[001]_{SL}||[301]_{magnetite}$, $[001]_{SL}||[100]_{magnetite}$. Overall the presented data provide a fundamental understanding of a mesocrystal formation mechanism and their structural evolution. Structure, composition, and magnetic properties of the synthesised nanoparticles are also characterized.

J. Brunner, Dr. E. Sturm (née Rosseeva), Prof. H. Cölfen
Physical Chemistry
University of Konstanz
Universitätsstraße 10, Box 714
78457 Konstanz, Germany
E-mail: elena.sturm@uni-konstanz.de;
helmut.coelfen@uni-konstanz.de

Dr. I. A. Baburin
Theoretical Chemistry
TU Dresden
Bergstrasse 66b, D-01062 Dresden, Germany

S. Sturm
Institute of Structure Physics
Triebenberg Laboratory for High-Resolution Electron Microscopy and Holography
TU Dresden
Zum Triebenberg 50, 01328 Dresden, Germany

Dr. K. Kvashnina, Dr. A. Rossberg
Rossendorf Beamline at ESRF – The European Synchrotron
CS40220, 38043 Grenoble Cedex 9, France

Dr. K. Kvashnina, Dr. A. Rossberg
Helmholtz Zentrum Dresden-Rossendorf (HZDR)
Institute of Resource Ecology
P.O. Box 510119, 01314 Dresden, Germany

Dr. T. Pietsch, S. Andreev
Department of Physics
University of Konstanz
Universitätsstraße 10, Box 714, 78457 Konstanz, Germany

1. Introduction

The inherent tendency of nanoparticles for aggregation and self-assembly processes represents a great opportunity to perform bottom up generation of novel nanostructured materials with controlled structure and complex functionality.[1–6] In addition, particle mediated nonclassical crystallization has been recognized to be of increasing importance as crystallization pathway in recent years.[7,8] In contrast to isotropic spherical nanoparticles, which self-assemble into a close-packed superlattice with random crystallographic orientation of the building blocks (colloidal crystal), nonspherical nanocrystals can generate much more complex superlattices (so-called mesocrystals) composed of building blocks with specific crystallographic orientation.[8–13] Building on the definition of a "crystal" given by IUCr,[14] we defined mesocrystals as "a nanostructured material with a defined long-range order on the atomic scale, which can be inferred from the existence of an essentially sharp wide angle diffraction pattern (with sharp Bragg peaks) together with clear evidence that the material consists of individual nanoparticle building units."[10]

One common approach to design mesocrystalline materials is the controlled self-assembly of nanoparticles with defined morphology and narrow size distribution. Magnetic nanoparticles allow additionaly to control the self-assembly process due to the internal dipolar magnetic attraction between the particles as well as by an external magnetic field. Therefore, iron oxide nanoparticles are one of the promising building blocks for the generation of mesocrystalline materials with different structure and functionality.[10,15–20] Furthermore, mesocrystals built up from nanometer-sized superparamagnetic nanoparticles should demonstrate more efficient magnetization than that of the individual nanoparticles due to specific crystallographic alignment of nanoparticles.[21,22] Thus collective and emergent properties can arise. This also provides the possibility to generate magnetic materials on the micrometer scale with controlled physical properties simply by controlling the size of individual building blocks and their arrangements within the superlattices, which would be impossible to achieve for the bulk material for the given mesocrystal size.

One way to synthesize ferrofluids is the large-scale synthesis of iron oxide nanoparticles via thermal decomposition of an

iron oleate precursor, established by Hyeon and co-workers in 2004, that still gains high interest in research.[23] The developed heating-up synthesis led to nanoparticles different in chemical composition, but highly monodisperse in size and shape.[24–27] Nowadays, a lot of researchers adopted the synthesis protocol for producing iron oxide nanocrystals with different size and shape via decomposition of an iron oleate precursor.[17–20] Unfortunately, the relevant literature is mostly lacking a full characterization of the nanoparticles, researchers often claim that either magnetite or maghemite is synthesized, without providing clear structural evidences. It is, nevertheless, an essential need to clearly identify the resulting material, especially for engineering or medical applications.[17–19,28,29] Indeed especially in case of nanoparticles, it is hard to distinguish between magnetite and maghemite compounds using diffraction techniques, due to the similarities of their crystal structures exhibiting the inverse spinel type.[30,31] However, both minerals are different in physical properties. The bulk maghemite (2 eV) and magnetite (0.1 eV) are semiconductors with a band gap less than 5 eV.[32,33] The saturation magnetization of magnetite is slightly higher compared to maghemite.[34,35] Due to these differences of the electronic and magnetic properties, both compounds can be used differently in various industrial applications.

Therefore, the information about the exact composition of nanoparticles is essential not only for basic research but also for materials design and application. The authors of the original publication[23,36,37] used XANES (X-ray absorption near edge structure) and claim that the ratio between Fe^{2+} and Fe^{3+} varies depending on the size of the resulting nanoparticles. The examinations exposed, that when nanoparticles reach sizes around 8 nm, magnetite is the dominating phase within the nanoparticles. Although only Fe^{3+} ions are used in the iron (III) oleate precursor material, it is proposed that an elimination of carbon dioxide of the precursor and surfactant molecule leads to the reduction of Fe^{3+} to Fe^{2+} ions. However, these results are inconsistent with the analyses with Mößbauer spectroscopy on nanoparticles with sizes around 15 nm.[38] Mößbauer spectroscopy is a reliable method to identify Fe^{3+} and Fe^{2+} ions and Salazar-Alvarez et al. claimed the nanoparticles synthesized via thermal decomposition were maghemite nanoparticles. Based on almost the same synthesis method the analysis of the nanoparticles differs enormously, therefore every time it is very important to determine the composition of the nanoparticles.

In the past years, we have prepared and structurally characterized a large variety of inorganic–organic composite mesocrystals (incl. biomimetic materials and nanoparticle self-assemblies).[10,11,13,39–41] In order to classify the material as a mesocrystal it is necessary to combine several techniques to clearly verify the long-range order at the atomic scale (in at least one crystallographic direction) as well as the existence of nanoparticles in the entire solid-state material (e.g., by combining electron microscopy imaging and diffraction techniques). One of our recent examples includes the detailed structural characterization of self-assembled mesocrystalline

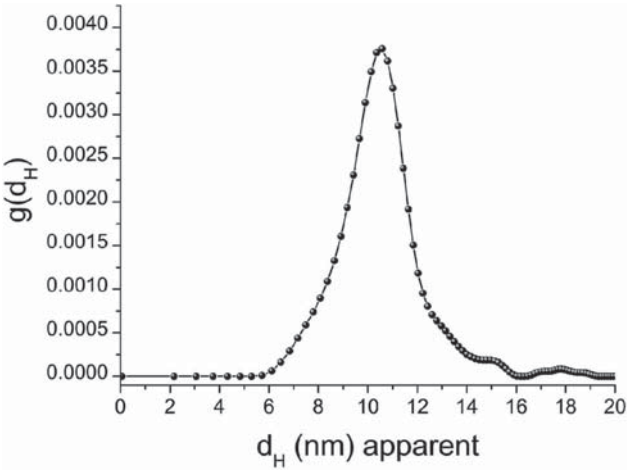

Figure 1. Size distribution of synthetic iron oxide nanoparticles (NPs) stabilized by oleic acid molecules obtained using analytical ultracentrifugation (AUC).

materials using the combination of advanced electron microscopy techniques (performed in collaboration with Simon et al. and Eychmüller and co-workers).[40,41] In this study we were able to determine the orientational relations between the PbS nanocrystals (stabilized by oleic acid molecules) within ordered 2D and 3D PbS mesocrystalline nanoparticle self-assemblies and also to develop atomistic models suitable for a detailed description of the structures of these mesocrystals. Furthermore, we proposed also a phenomenological model, which provides a clear explanation of specific structuring within ordered superlattice arrays depending on the degree and thickness of organic coverage of polyhedral nanoparticles.[41]

Another very efficient analytical tool for characterization of self-assembled mesocrystalline materials is high-resolution synchrotron-based small/wide-angle X-ray scattering (SAXS/WAXS) (including in situ time-resolved grazing incidence small-angle X-ray scattering and grazing incidence wide-angle X-ray scattering).[42–45] These techniques are developing very fast within the last years and are allowing to determine the packing arrangement and orientational order of nanoparticles not only within solid mesocrystals but also to track in situ their structural evolution during the self-assembly process.[46]

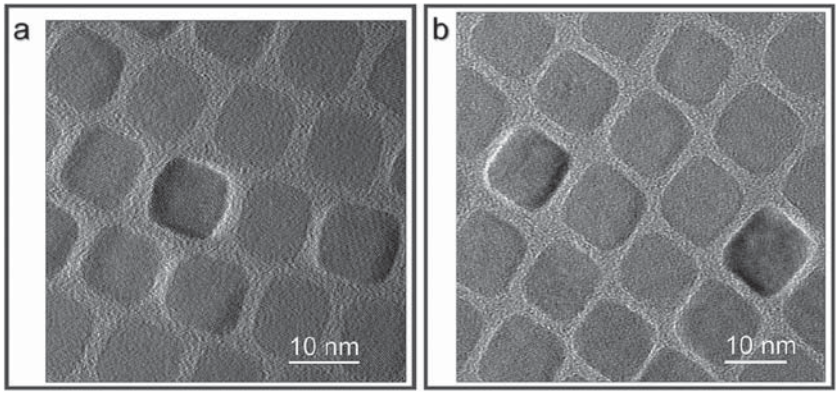

Figure 2. Cs-corrected HRTEM images of iron oxide truncated nanocubes. a) Sample batch I. b) Sample batch II.

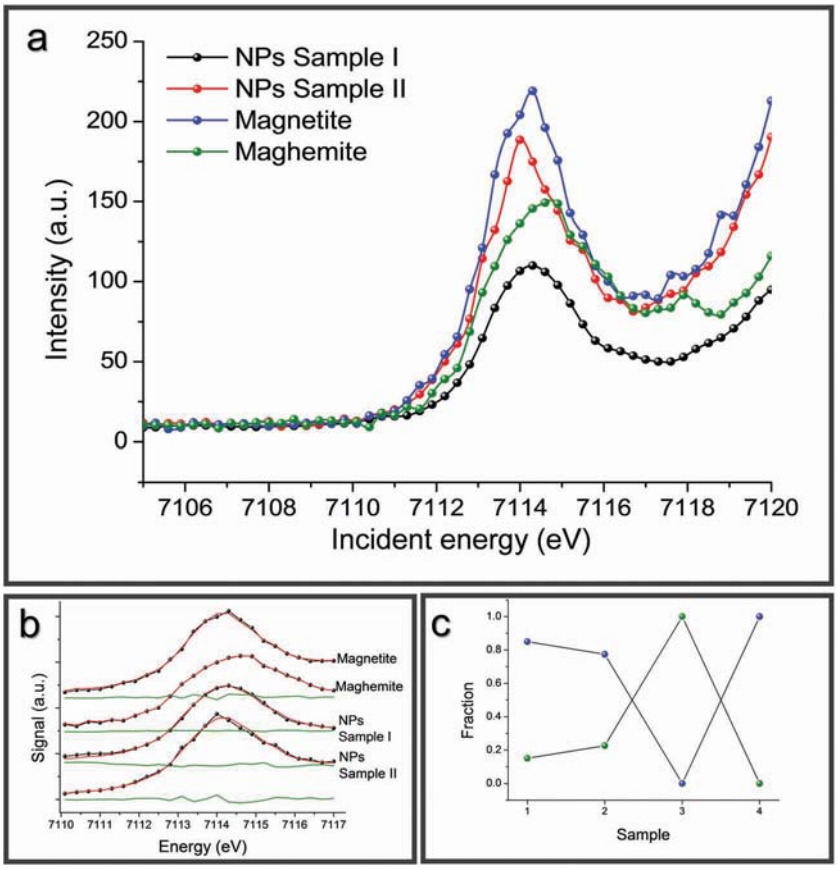

Figure 3. a) Comparison of the Fe-K pre-edge HERFD-XANES spectra of the iron oxide nanoparticles (NPs) samples and reference bulk systems: magnetite (Fe_3O_4) and maghemite (Fe_2O_3). b) Results of iterative transformation factor analysis (spectra decomposition): Black line – experimental data (normalized to L2-norm). Red – reproduction of the experimental data by linear combination of two spectral components (maghemite and magnetite). Green–residual between data and reproduction. c) Fractions of component 1 (maghemite Fe_2O_3, green dots) and component 2 (magnetite Fe_3O_4, blue dots) in the samples 1- 4 (1 – NPs sample II, 2- NPs sample I, 3- bulk Fe_2O_3, and 4 – bulk Fe_3O_4).

Our present study is focussed on synthesis and detailed characterization of 2D and 3D mesocrystalline films produced by self-assembly of iron oxide (magnetite) truncated nanocubes. The approach we are using in our study aims to determine the orientational relations between the nanocrystals using the combination of electron microscopy techniques within the superlattice and also to develop atomistic models suitable for a detailed description of the structures of the 2D and 3D colloidal superlattices (mesocrystals) and their structural relation. These data are very important for the fundamental understanding of the mesocrystal formation mechanism and structuring. Furthermore, we performed detailed structural characterisation of iron oxide nanoparticles and examined their magnetic properties.

2. Results and Discussion

2.1. Nanoparticle Characterization

Iron oxide nanoparticles were successfully prepared using the thermal decomposition of an iron(III) oleate precursor. Analytical ultracentrifugation (AUC) indicates a quite narrow size distribution of nanoparticles (**Figure 1**, $d_H = 10.4 \pm 1.2$ nm) which is additionally confirmed by high resolution transmission electron microscopy (HRTEM) and scanning electron microscope (SEM) (see below, Figures 4, 6, and 9). The inverse spinel crystal structure determined by HRTEM and electron diffraction can be attributed to both magnetite and maghemite. In order to define

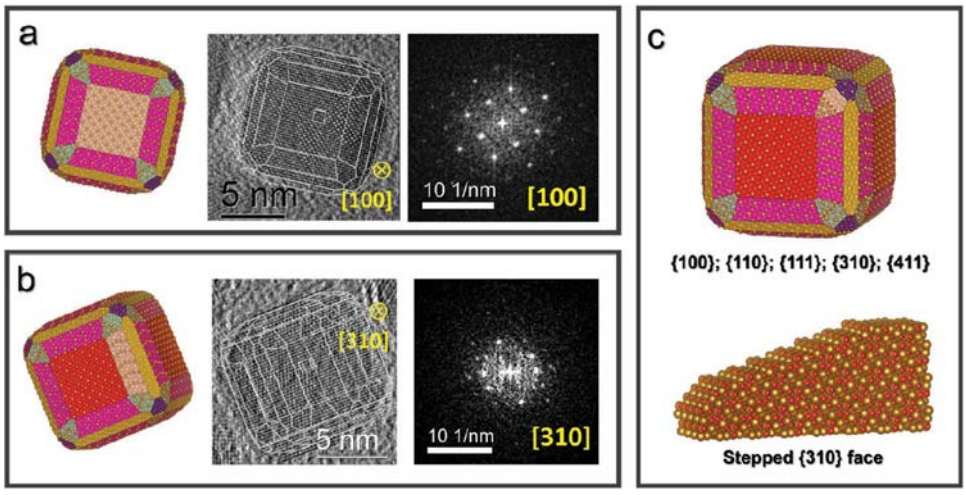

Figure 4. a,b) Cs-corrected HR-TEM images of nanoparticles (sample I) viewed along $[100]_{Fe3O4}$ and $[310]_{Fe3O4}$ and their corresponding FFTs (right) and projections of simulated truncated cubic shaped nanoparticles (left). c) Simulated idealized shape of magnetite nanocube slightly truncated by the {111}, {110}, {310}, and {114} faces and representation of stepped {310} face.

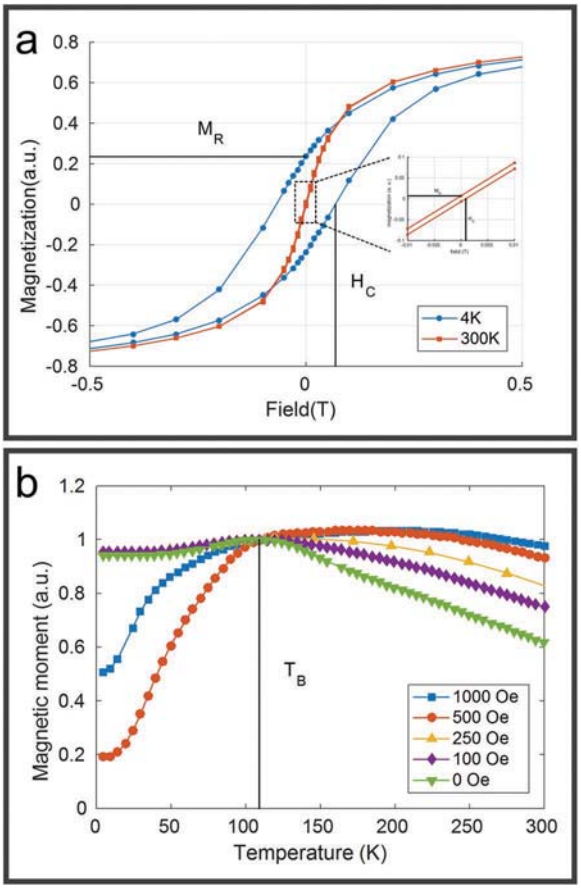

Figure 5. Magnetic properties of the magnetite nanoparticles (sample II). a) Hysteresis loops measured at 4 and 300 K showing the dependence of nanoparticle magnetization to the external magnetic field in *z*-direction. b) Temperature-dependent measurements of nanoparticle magnetic moment recorded at constant magnetic H-fields. The critical (blocking) temperature is $T_B = 110$ K.

the exact composition of the nanoparticles, high-energy-resolution fluorescence detection (HERFD)-XANES measurements of nanoparticles were performed (two sample batches (I) and (II) were examined). Spherical aberration corrected (Cs-corrected) HRTEM (**Figure 2**) shows that nanocubes from batch (I) are slightly smaller and slightly more truncated compared with nanocubes from batch (II). **Figure 3**a shows the pre-edge structures at the Fe K-edge for iron oxide nanoparticles in comparison with maghemite and magnetite bulk reference compounds. The energy position of the pre-edge maximum (around 7114.5 eV) and the intensity in the spectrum of iron oxide nanoparticles appears to be different from that of the maghemite and more close to that of magnetite reference compounds. On the other hand, the careful analysis of the recorded spectra also indicates the presence of a small amount of maghemite in the synthetic materials. Therefore, in order to determine the exact fraction of magnetite and maghemite the iterative transformation factor analysis[47] was used (which allows to decompose the spectral mixtures into the recorded spectra). Thus it was shown, that by using a linear combination of two components the spectra can be sufficiently reproduced (Figure 3b), so that the residual (Figure 3b, green line) is similar to the expected experimental error. The analysis shows that the first sample of iron oxide nanoparticles contains 77.4% of Fe_3O_4 and 22.6% of Fe_2O_3 components, while the sample II contains 85% of Fe_3O_4 and 15% of Fe_2O_3. The extracted spectra and the fractions of the components are shown in Figure 3a,c, respectively. Since it was shown that in both systems the dominating phase is magnetite, for the simplicity reason the indexing of all electron diffraction patterns, analysis of HRTEM images and atomistic simulations of nanoparticles and their self-assemblies were performed based on the magnetite crystal structure only.

The Cs-corrected HRTEM images of the nanoparticles recorded along different zone axes (**Figure 4**) clearly show that the morphology of the magnetite nanoparticles is very close to cubic shape, slightly truncated by the {111}, {110}, {310},

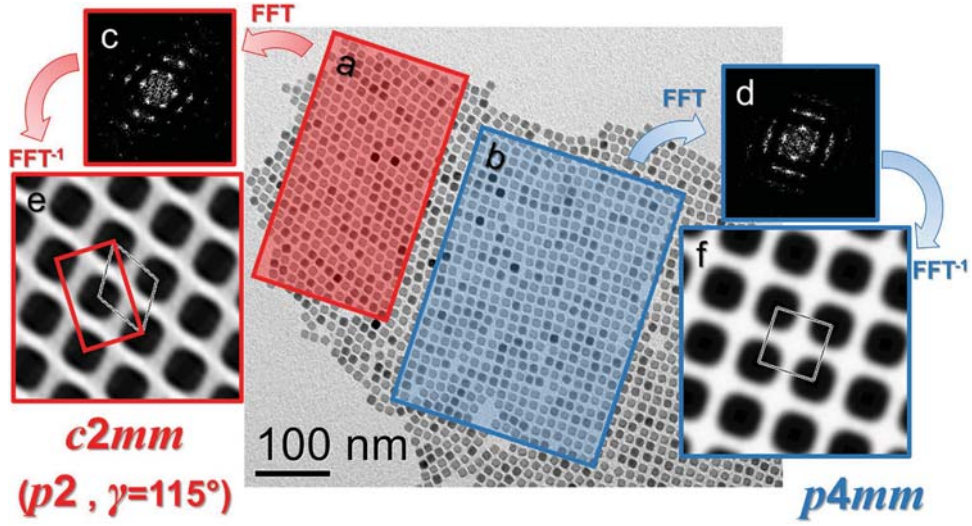

Figure 6. TEM image of self-assembled monolayer of magnetite nanoparticles (sample I) with coexisting structural domains exhibiting a) *c2mm* and b) *p4mm* symmetry. c) and d) FFT of areas (a) and (b), respectively. e) and f) zoomed filtered TEM images imposing *c2mm* (*p2*) and *p4mm* plane group symmetries taken from areas (a) and (b), respectively.

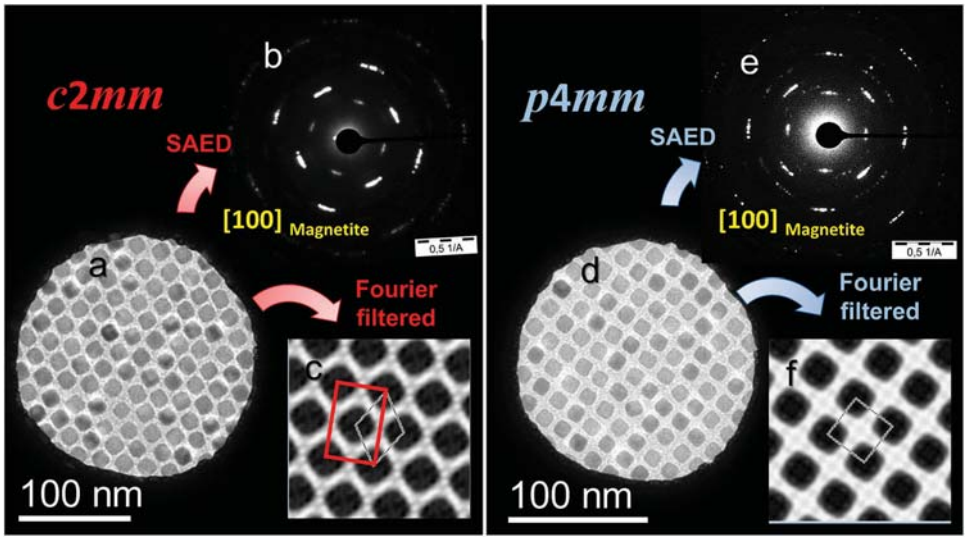

Figure 7. a,d) TEM-images of a self-assembled monolayer of magnetite nanoparticles with structural domains exhibiting a) *c2mm* and d) *p4mm* symmetry. b) and e) selected area electron diffraction pattern recorded from areas (a) and (d), respectively. The texture-like pattern can be indexed as [100] Magnetite zone axis. The azimuthal spread of the reflections indicates a slight orientational mismatch of nanoparticles. c) and f) Zoomed filtered TEM images imposing *c2mm* (*p2*) and *p4mm* plane group symmetries taken from areas (a) and (d), respectively.

and {114} faces. Therefore, the magnetite nanocubes have significantly smoothed vertices and edges as well as stepped basal facets. Figure 4 displays [100] and [310] orientations of a simulated magnetite nanoparticle in comparison with projected Cs-corrected HRTEM images of nanoparticles recorded along the same zone axis as determined from the fast Fourier transforms (FFT).

Since the synthesized nanoparticles are around 10 nm, they demonstrate superparamagnetic behavior at room temperature (**Figure 5**). A magnetic phase transition for the synthesized nanoparticles is observed around 110 K (Figure 5b), corresponding to the blocking temperature. Therefore, the hysteresis loops (Figure 5a) recorded at 4 and 300 K show significantly different behavior for remanence and coercivity and can be referred to ferrimagnetic and superparamagnetic properties of nanoparticles, respectively. These results are consistent with the analyses of Park et al. and Faure et al.[18,21]

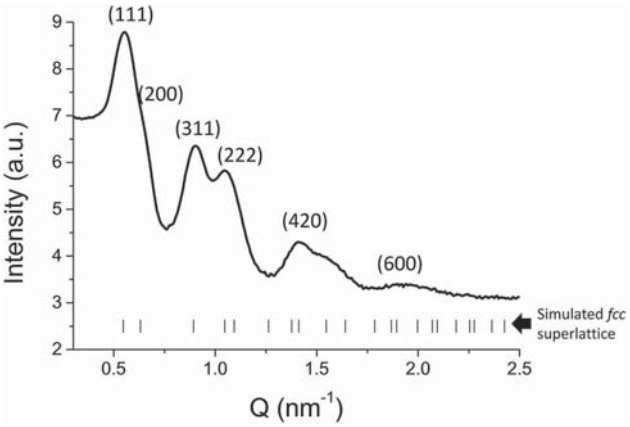

Figure 8. SAXS pattern recorded from magnetite nanoparticle self-assemblies, indicating the fcc (a = 20 nm) structure of 3D superlattices.

2.2. Mesocrystalline Nanoparticles Self-Assemblies

The preparation of 2D and 3D mesocrystalline films was performed directly on grids for transmission electron microscopy (TEM) by slow evaporation of the nanoparticle dispersion in toluene using an excess of surfactant. The TEM images of the 2D self-assemblies show the coexistence of two structurally different domains (**Figure 6**). The first one has the topology of a square lattice (*p4mm*, a = 14.5 nm, Figure 6b,d,f) while the second one represents a distorted close-packed arrangement (*p2*, $a = b$ = 14.8 nm, $\gamma \sim 115°$ this oblique cell can be also described in a *c2mm* plane group (a = 25.0 nm, b = 15.9 nm) Figure 6a,c,e). This observation is consistent with previous experimental observations and theoretical modeling of cubic packing.[16,48,49] Selected area electron diffraction (SAED) (**Figure 7**) confirms that all nanocubes in both patterns have

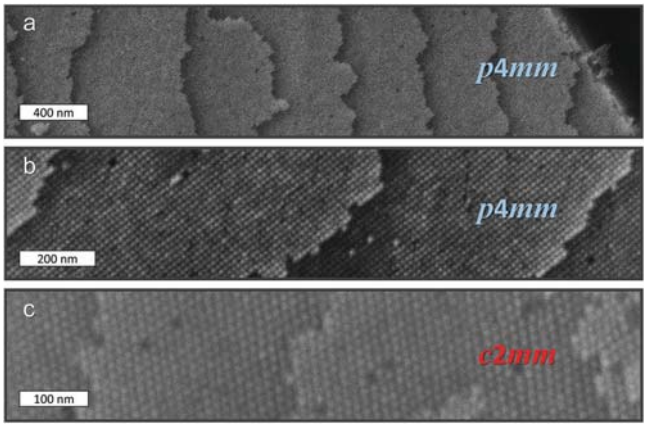

Figure 9. SEM images of multilayered films of magnetite nanoparticle self-assemblies exhibiting a,b) *p4mm* and c) *c2mm* symmetries of stacked layers.

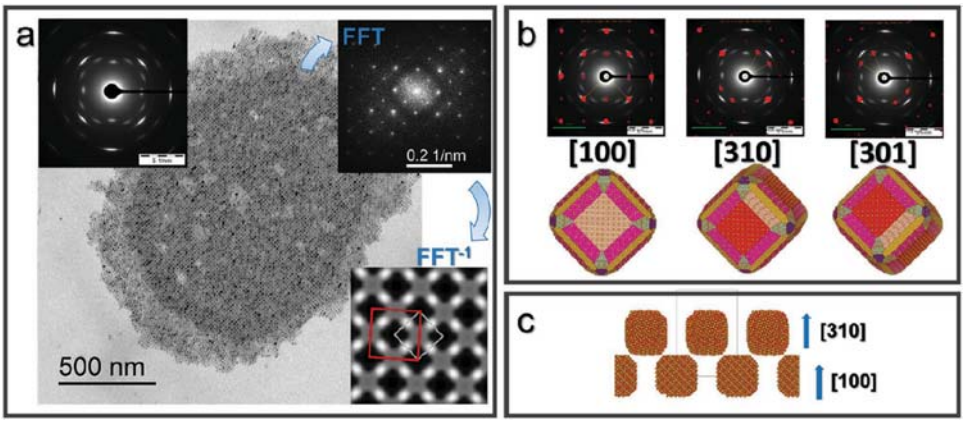

Figure 10. a) TEM image of self-assembled multilayer of magnetite nanoparticles (sample I) with fcc superstructure and corresponding SAED pattern (top left), FFT (top right), and zoomed filtered TEM image (bottom right), obtained along [100] direction of the superlattice and showing projected *p4mm* symmetry. b) SAED pattern overlaid by simulated electron diffraction patterns of magnetite in [100], [310] and [301] zone axis and projected modelled truncated nanocubes in respective orientations. c) Schematic illustration of stacking of squared monolayers within fcc superlattice. Showing the changes in orientation of nanocubes in second layer, allowing for more efficient space filling (bump-to-hollow principle).

the same orientation, with {100} faces lying on the substrate. On the way toward the formation of multilayered films, nanoparticles tend to arrange in a slightly distorted face-centered cubic (fcc) superlattice. This is confirmed by SAXS measurements (**Figure 8**, sp. gr. $Fm\bar{3}m$, a = 20 nm). Unfortunately, broad reflections do not allow us to determine the kind of superlattice distortion (e.g., tetragonal or rhombohedral deformations), as described earlier in similar systems.[2,10,15,16,20,43,48,50,51] The SEM images (**Figure 9**) visualize the stacking of *p4mm* and *c2mm* monolayers forming 3D self-assembled films. The TEM image in **Figure 10**a is illustrating the projection of a 3D superlattice formed by stacking of monolayers with *p4mm* symmetry. This projection corresponds to the [100] zone axis of an fcc superlattice and is shown as a projected unit cell (red frame) in Figure 10a (bottom right), the calculated lattice parameters (a_{fcc} = 20.4 nm) are in a good agreement with SAXS results (Figure 8). The projection of the related *bct* cell is shown as a white frame (Figure 10a (bottom right), $a_{bct} = a_{fcc}/\sqrt{2}$ = 14.5 nm, $c_{bct} = a_{fcc}$ = 20.4 nm). The SAED pattern taken from the square domain of a multilayer shows a texture-like pattern (Figure 10a, top left), which is different from that of a monolayer with the same symmetry (Figure 7e). Additional reflections can be indexed as [310] and [301] zone axes of magnetite, indicating that some particles within adjacent layers lie on (310) and (301) faces (Figure 10b). The occurrence of nanoparticles in different orientation allows for more efficient space filling (Figure 10c), in line with the well-known packing principle

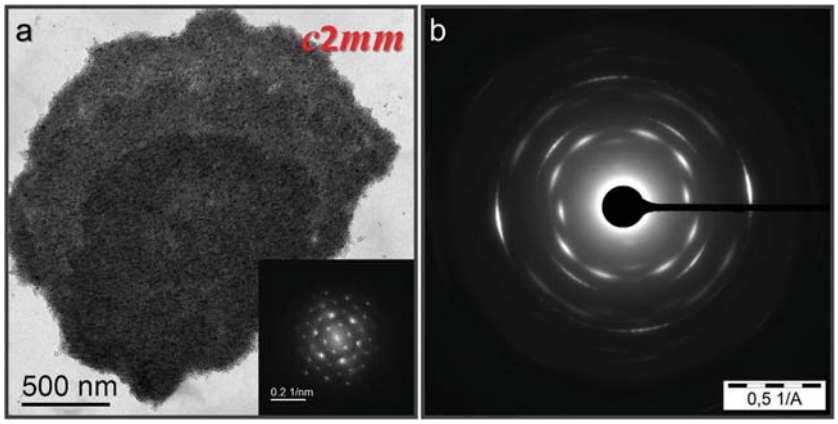

Figure 11. a) TEM image of self-assembled multilayer of magnetite nanoparticles (sample I) and corresponding FFT (bottom right) showing projected *c2mm* symmetry. b) SAED pattern of (a).

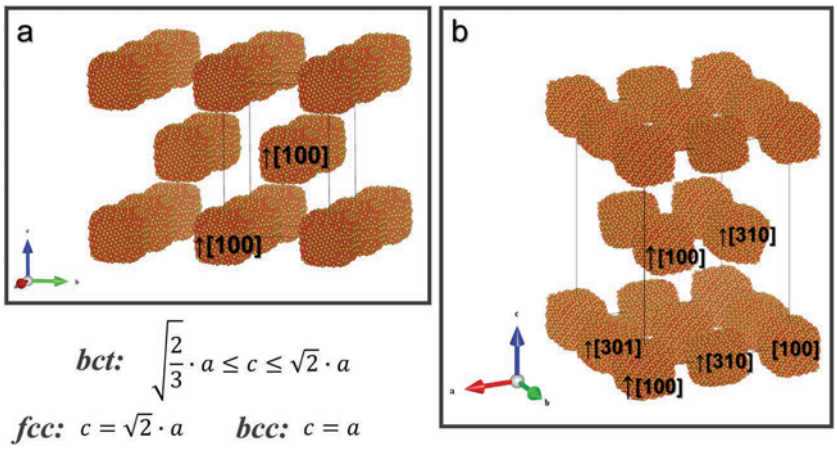

Figure 12. a) Simplified and b) realistic structural models of 3D self-assemblies. a) Nanoparticles oriented along [100] exclusively within stacked squared layers. b) Nanoparticles oriented along [100], [310], and [301] within stacked squared layers.

"bump-to-hollow" in molecular crystals.[52] The term "bump-to-hollow" (or "bump into hollow") is widely used to describe the packing of molecules in a crystal (see e.g., ref. [7]). It simply means that "convexities" of one molecule fit into the "concavities" of another. Similar orientation relations for nanoparticles can be derived from the wide-angle electron diffraction pattern of 3D films composed of layers with *c2mm* symmetry (**Figure 11**). Both structures can be classified as mesocrystals.

To gain more insight into the atomistic structure of the superlattices, we constructed a series of models representing 2D and 3D mesocrystals and simulated electron diffraction patterns in small and wide-angle regions. For computational efficiency, the size of the model magnetite cluster was set to ≈4 nm, which is approximately 2.5 times smaller than the actual size of the nanoparticle. The clusters were arranged in square nets (symmetry *p4mm*, the scaled distance between centres of neighbouring nanoparticles is 6 nm). The square nets were then stacked in a way so as to approximate an overall fcc packing of the nanoparticles (**Figure 12**). The possibility to have different orientations of nanoparticles relative to the superlattice ($[001]_{SL}||\ [310]_{magnetite}$, $[001]_{SL}||[301]_{magnetite}$, $[001]_{SL}\ ||\ [100]_{magnetite}$) was carefully examined (**Figures** 12 and **13**). Additionally, we built up and compared the structures of individual monolayers with *p4mm* and *c2mm* symmetry (Figure 13), the latter model was formally described in an oblique cell of *p2* ($\gamma = 115°$). The comparison of simulated and observed patterns shows a very nice agreement (**Figure 14**) confirming our assumptions on the topology of the superlattices and preferred orientations of nanoparticles.

3. Conclusion

In summary, we performed a synthesis of iron oxide truncated nanocubes stabilized by oleic acid molecules and produced 2D and 3D self-assembled mesocrystaline films thereof. As we have demonstrated by detailed structural analysis, the dominant phase of the nanocubes is magnetite. The morphology of the magnetite nanoparticles, crucial for understanding the packing arrangement and the orientational order in 2D and 3D superlattices, is very close to a cube truncated by {111}, {110}, {310}, and {114} faces.

Already in the 2D case, two distinct superstructures of magnetite nanocubes with *p4mm* and *c2mm* layer symmetries and the same orientational order can be observed (with $[100]_{magnetite}$ perpendicular to substrate). The 3D structure can be approximated by slightly distorted fcc superlattice. As we have shown, the orientational order of nanoparticles within stacked monolayers becomes even more complex on the way to 3D superstructures. Namely orientational order is determined by the shape of the nanoparticles (with the following orientational relations: $[001]_{SL}||[310]_{magnetite}$, $[001]_{SL}||[301]_{magnetite}$, $[001]_{SL}||[100]_{magnetite}$). Therefore, the nanoparticles can achieve a more efficient arrangement by following the "bump-to-hollow" packing principle.[52]

The atomistic modelling not only verifies the proposed mesocrystal structures but also provides great insight into fundamental principles of structuring of 2D and 3D mesocrystals.

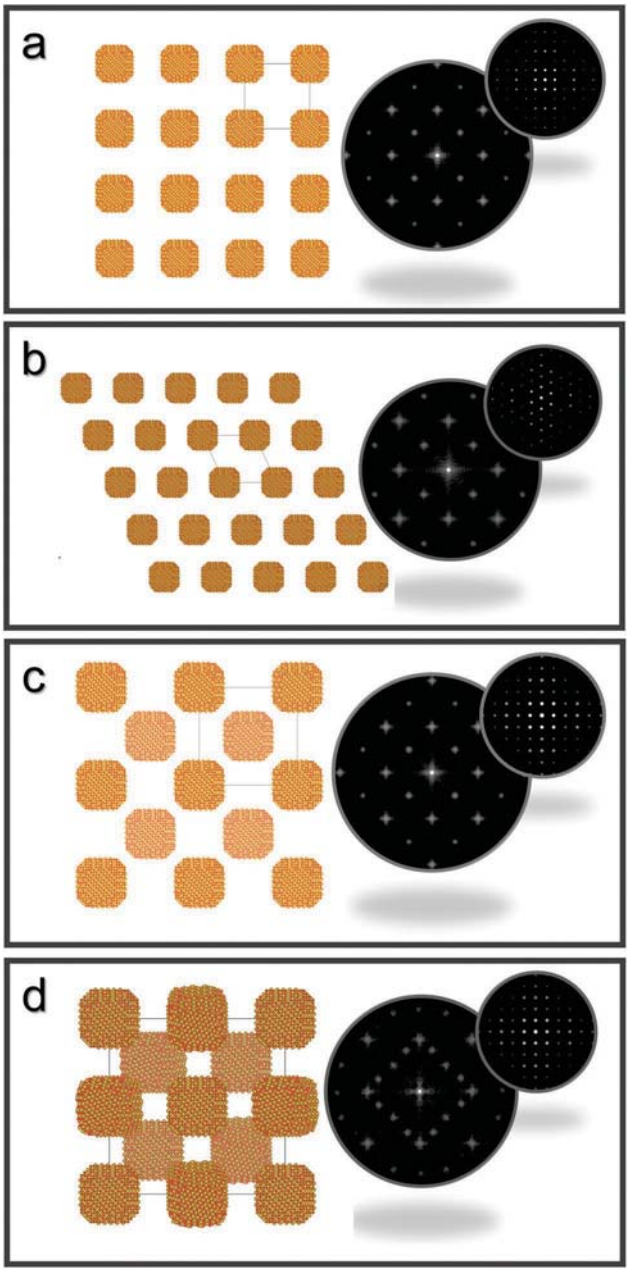

Figure 13. Atomistic models of a,b) 2D and c,d) 3D magnetite nanoparticle superlattices with corresponding simulated wide (left) and small (right) angle electron diffraction patterns. a) Squared and b) oblique monolayers with uniform coaxial [100] magnetite orientation. c,d) 3D superlattices shown in Figure 12 (a and b, respectively) projected along [001] direction.

4. Experimental Section

Synthesis of the Nanocubes: The synthesis of iron oxide nanocubes was followed according to literature by applying the heating-up method.[18,19,23,53] All chemicals were used as received. For the preparation of the iron (III) oleate precursor, iron (III) chloride (5.4 g, 20 mmol, 97%, Sigma-Aldrich), and sodium oleate (18.3 g, 60 mmol, 97%, Tokyo Chemical Industry) were heated up to reflux temperature in a mixture of Ethanol (40 mL), Hexane (70 mL), and purified water

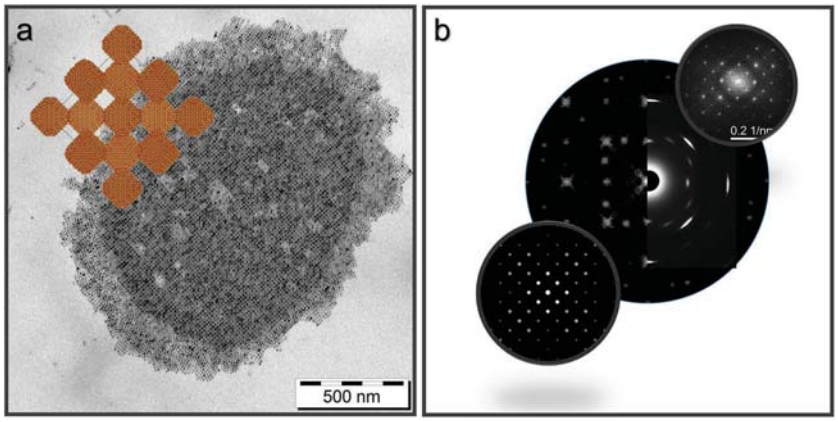

Figure 14. Comparison of experimental data and results of atomistic modeling (presented in Figure 12b). a) TEM image of self-assembled multilayer of magnetite nanoparticles with fcc structure along [001] and corresponding atomistic model (top left). b) Superposition of experimental (right) and simulated (left) wide and small angle electron diffraction patterns.

(30 mL). The resulting organic phase was washed with water and dried at 50 °C under vacuum. Afterward, Iron (III) oleate (9.08 g, 10 mmol), sodium oleate (0.436 g, 1.43 mmol), and oleic acid (0.453 mL, 1.43 mmol, 99%, Tokyo Chemical Industry) were solved in Octadecene (50 mL, 90%, Sigma-Aldrich) and heated up to 60 °C and dried under vacuum for 30 min. Using a heating ramp of 3 °C min^{-1}, the reaction mixture was heated up to reflux temperature. After 30 min at 320 °C the reaction mixture was cooled down to room temperature. Finally, the reaction mixture was washed with ethanol and toluene by centrifugation. The colloidal dispersion was stored in toluene.

Synthesis of the Mesocrystalline Films: The preparation of mesocrystals was performed via self-assembly with a slow evaporation of the nanoparticle dispersion using an excess of surfactant.[30] 300 µL of a nanoparticle dispersion with a concentration of 0.25 mg mL^{-1} were dried in 2 mL glass vessel containing a carbon-coated copper grid for transmission electron microscopy (London finder Science Services; CFLF400-Cu-UL). The concentration of the excess of the surfactant was 1.5 µL mL^{-1}.

Transmission Electron Microscopy: Two different TEM were used for the investigation—A Zeiss Libra120 with a 120 kV Lathanum hexaboride emitter and a Koehler illumination system reaching a resolution of 0.34 nm. The information limit was about 0.20 nm and an in-column OMEGA filter was installed. The Cs-corrected high resolution TEM imaging of the nanoparticles was performed using an FEI Tecnai F20/Cs-corrected TEM at 200 kV acceleration voltage. The analyses of the TEM images were realised by means of the Digital Micrograph (Gatan, USA) and CRISP (copyright Calidris, Sweden) software.

Scanning Electron Microscopy: The used SEM was a Zeiss CrossBeam 1540XB reaching a resolution of up to 1.1 nm at 20 kV the acceleration voltage can be changed from 0.1 to 30 kV. It was equipped with an SE2 and an InLens detector.

Small-Angle X-Ray Scattering: The SAXS measurements of the self-assembled nanoparticles were performed by means of a Bruker AXS Nanostar diffractometer using Cu Kα radiation. The analysis of SAXS pattern was performed using Scatter (Version 2.5, 03/2011) software.[54]

X-Ray Absorption Spectroscopy: The experiment has been performed at the Rossendorf beamline – BM20 at the European Synchrotron Radiation Facility (ESRF) in Grenoble. The incident energy was selected using the ⟨111⟩ reflection from a double Si crystal monochromator. Rejection of higher harmonics was achieved by two Si mirrors at an angle of 2.5 mrad relative to the incident beam. XANES spectra were measured in HERFD mode using an X-ray emission spectrometer.[55] Sample, analyzer crystal, and photon detector (silicon drift diode) were arranged in a vertical Rowland geometry for X-ray emission spectrometer. The Fe HERFD spectra at the K edge were obtained by recording the maximum intensity of the Fe $K\beta_1$ emission line (7059.3 eV) as a function of the incident energy. The emission energy was selected using the ⟨620⟩ reflection of the one spherically bent Ge crystal analyzers (with 1 m bending radius) aligned at 79° Bragg angle. The intensity was normalized to the incident flux. A combined (incident convoluted with emitted) energy resolution of 1.8 eV was obtained as determined by measuring the full width at half maximum of the elastic peak. Reference material (Fe foil) has been used as energy calibration for the absorption edge. Radiation damage induced by an X-ray beam was carefully checked by taking few HERFD-XANES scans of the few seconds collection time. The powder references (Fe_2O_3 and Fe_3O_4, provided by ESRF) and iron oxide nanoparticle samples were sealed in the Kapton films with a thickness of 25 µm. The powder samples of iron oxide nanoparticles were removed from the inert atmosphere just before the measurements with a delay time of 10 min.

Chemical Analysis: The content of oleic acid in synthetic nanoparticles was calculated on the basis of carbon concentration which was determined by means of CHN-Analyser Vario Micro Cube of Elementar Company.

Analytical Ultracentrifugation: The AUC measurements were performed on an Optima XL I (Beckman Coulter, Palo Alto, CA, United States) using Rayleigh interference optics and 12 mm double sector titanium centrepieces (Nanolytics, Potsdam, Germany). Nanoparticles dispersions in toluene were investigated at 20 °C and 7000 rpm. In order to calculate the hydrodynamic diameter of nanoparticles, the real density of magnetite nanoparticles stabilized by oleic acid (4.299 g cm^{-3}) was estimated by taking into account that the oleic acid content was around 20 wt% (based on the results of chemical analysis).

Structure Modeling: Simulations were performed in line with our former works. The structure of an individual nanoparticle was modelled by a cluster with the habit of a truncated cube (additional faces were chosen to be {111}, {110}, {310}, and {114}, as suggested by HRTEM data) cut from a magnetite structure Fe_3O_4 (sp. gr. $Fd\bar{3}m$) using the VESTA 3 software.[56] VESTA 3 was also used to visualize structure models. 2D and 3D superlattices were constructed from individual clusters (for further details see main text) and electron diffraction patterns were simulated using the program JEMS. Cif-files of model structures can be obtained from the authors upon request.

Superconducting Quantum Interference Device: The analysis of iron oxide powder (1.24 mg) was performed using a SQUID, MPMS XL of Quantum design. For the visualization of the dependence of magnetization to the external magnetic field in *z*-direction hysteresis loops were measured at 4 and 300 K in a range of –3.5 to 3.5 T. The critical (blocking) temperature T_B was determined using temperature dependent measurements at different, constant magnetic H-fields. The used temperature interval was 4–300 K and the magnetic fields applied were fixed to 0 T, 10 mT, 25 mT, 50 mT, and 100 mT.

Acknowledgements

The authors thank Dr. Marina Krumova, Alexander Klaiber, and Rose Rosenberg for experimental support and fruitful discussions. They also thank the DFG (Deutsche Forschungsgemeinschaft) for support of this project within the SFB 1214. T.P. and E.S. thank the Zukunftskolleg at the University of Konstanz for financial support.

[1] M. V. Kovalenko, L. Manna, A. Cabot, Z. Hens, D. V. Talapin, C. R. Kagan, V. I. Klimov, A. L. Rogach, P. Reiss, D. J. Milliron, P. Guyot-Sionnnest, G. Konstantatos, W. J. Parak, T. Hyeon, B. A. Korgel, C. B. Murray, W. Heiss, *ACS Nano* **2015**, *9*, 1012.
[2] Z. Quan, J. Fang, *Nano Today* **2010**, *5*, 390.
[3] D. V. Talapin, *MRS Bull.* **2012**, *37*, 63.
[4] D. Vanmaekelbergh, *Nano Today* **2011**, *6*, 419.
[5] T. Wang, D. LaMontagne, J. Lynch, J. Zhuang, Y. C. Cao, *Chem. Soc. Rev.* **2013**, *42*, 2804.
[6] S. Y. Zhang, M. D. Regulacio, M. Y. Han, *Chem. Soc. Rev.* **2014**, *43*, 2301.
[7] J. D. Dunitz, in *Implications of Molecular and Materials Structure for New Technologies* (Eds: J. A. K. Howard, F. H. Allen, G. P. Shields), Springer, Dordrecht, Netherlands **1999**, p. 175.
[8] H. Cölfen, M. Antonietti, *Mesocrystals and Nonclassical Crystallization*, John Wiley & Sons, Chichester, UK **2008**.
[9] L. Bahrig, S. G. Hickey, A. Eychmuller, *Crystengcomm* **2014**, *16*, 9408.
[10] L. Bergstrom, E. V. Sturm, G. Salazar-Alvarez, H. Cölfen, *Acc. Chem. Res.* **2015**, *48*, 1391.
[11] H. Cölfen, M. Antonietti, *Angew. Chem., Int. Ed.* **2005**, *44*, 5576.
[12] M. G. Ma, H. Cölfen, *Curr. Opin. Colloid Interface Sci.* **2014**, *19*, 56.
[13] R. Q. Song, H. Colfen, *Adv. Mater.* **2010**, *22*, 1301.
[14] *Acta Crystallographica Section A* **1992**, *48*, 922.
[15] M. Agthe, K. Hoydalsvik, A. Mayence, P. Karvinen, M. Liebi, L. Bergstrom, K. Nygard, *Langmuir : ACS J. Surf. Colloids* **2015**, *31*, 12537.
[16] M. Agthe, E. Wetterskog, J. Mouzon, G. Salazar-Alvarez, L. Bergstrom, *Crystengcomm* **2014**, *16*, 1443.
[17] A. Ahniyaz, Y. Sakamoto, L. Bergstrom, *Proc. Nat. Acad. Sci. USA* **2007**, *104*, 17570.
[18] Y. I. Park, Y. Piao, N. Lee, B. Yoo, B. H. Kim, S. H. Choi, T. Hyeon, *J. Mater. Chem.* **2011**, *21*, 11472.
[19] G. Singh, H. Chan, A. Baskin, E. Gelman, N. Repnin, P. Kral, R. Klajn, *Science* **2014**, *345*, 1149.
[20] G. Singh, H. Chan, T. Udayabhaskararao, E. Gelman, D. Peddis, A. Baskin, G. Leitus, P. Kral, R. Klajn, *Faraday Discuss.* **2015**, *181*, 403.
[21] B. Faure, E. Wetterskog, K. Gunnarsson, E. Josten, R. P. Hermann, T. Bruckel, J. W. Andreasen, F. Meneau, M. Meyer, A. Lyubartsev, L. Bergstrom, G. Salazar-Alvarez, P. Svedlindh, *Nanoscale* **2013**, *5*, 953.
[22] J. P. Ge, Y. X. Hu, M. Biasini, W. P. Beyermann, Y. D. Yin, *Angew. Chem.-Int. Ed.* **2007**, *46*, 4342.
[23] J. Park, K. J. An, Y. S. Hwang, J. G. Park, H. J. Noh, J. Y. Kim, J. H. Park, N. M. Hwang, T. Hyeon, *Nat. Mater.* **2004**, *3*, 891.
[24] W. Baaziz, B. P. Pichon, Y. Liu, J.-M. Grenèche, C. Ulhaq-Bouillet, E. Terrier, N. Bergeard, V. Halté, C. Boeglin, F. Choueikani, M. Toumi, T. Mhiri, S. Begin-Colin, *Chem. Mater.* **2014**, *26*, 5063.
[25] B. Bateer, C. Tian, Y. Qu, S. Du, Y. Yang, Z. Ren, K. Pan, H. Fu, *Dalton Trans.* **2014**, *43*, 9885.
[26] J. C. Boyer, F. Vetrone, L. A. Cuccia, J. A. Capobianco, *J. Am. Chem. Soc.* **2006**, *128*, 7444.
[27] A. Shavel, L. M. Liz-Marzan, *Phys. Chem. Chem. Phys.* **2009**, *11*, 3762.
[28] A. T. Ngo, J. Richardi, M. P. Pileni, *Phys. Chem. Chem. Phys. : PCCP* **2013**, *15*, 10666.
[29] H. R. Zhou, K. Tao, Y. Q. Sui, K. Sun, *Physica E* **2011**, *44*, 597.
[30] M. E. Fleet, *J. Solid State Chem.* **1986**, *62*, 75.
[31] R. Grau-Crespo, A. Y. Al-Baitai, I. Saadoune, N. H. De Leeuw, *J. Phys.-Condens. Matter* **2010**, *22*, 255401.
[32] R. M. Cornell, U. Schwertmann, in *The Iron Oxides*, Wiley-VCH, Weinheim, Germany, **2004**, p. 111.
[33] M. I. Litter, M. A. Blesa, *Can. J. Chem.* **1992**, *70*, 2502.
[34] J. M. D. Coey, in *Iron in Soils and Clay Minerals* (Eds: J. W. Stucki, B. A. Goodman, U. Schwertmann), Springer, Dordrecht, Netherlands **1988**, p. 397.
[35] H. C. Soffel, in *Paläomagnetismus und Archäomagnetismus*, Springer, Berlin **1991**, p. 7.
[36] B. H. Kim, M. J. Hackett, J. Park, T. Hyeon, *Chem. Mater.* **2014**, *26*, 59.
[37] B. H. Kim, K. Shin, S. G. Kwon, Y. Jang, H.-S. Lee, H. Lee, S. W. Jun, J. Lee, S. Y. Han, Y.-H. Yim, D.-H. Kim, T. Hyeon, *J. Am. Chem. Soc.* **2013**, *135*, 2407.
[38] G. Salazar-Alvarez, J. Qin, V. Sepelak, I. Bergmann, M. Vasilakaki, K. N. Trohidou, J. D. Ardisson, W. A. Macedo, M. Mikhaylova, M. Muhammed, M. D. Baro, J. Nogues, *J. Am. Chem. Soc.* **2008**, *130*, 13234.
[39] R. Kniep, P. Simon, E. Rosseeva, *Crystal Res. Technol.* **2014**, *49*, 4.
[40] P. Simon, L. Bahrig, I. A. Baburin, P. Formanek, F. Roeder, J. Sickmann, S. G. Hickey, A. Eychmueller, H. Lichte, R. Kniep, E. Rosseeva, *Adv. Mater.* **2014**, *26*, 3042.
[41] P. Simon, E. Rosseeva, I. A. Baburin, L. Liebscher, S. G. Hickey, R. Cardoso-Gil, A. Eychmüller, R. Kniep, W. Carrillo-Cabrera, *Angew. Chem. Int. Ed.* **2012**, *51*, 10776.
[42] R. Li, K. Bian, T. Hanrath, W. A. Bassett, Z. Wang, *J. Am. Chem. Soc.* **2014**, *136*, 12047.
[43] R. Li, K. Bian, Y. Wang, H. Xu, J. A. Hollingsworth, T. Hanrath, J. Fang, Z. Wang, *Nano Lett.* **2015**, *15*, 6254.
[44] R. Li, J. Zhang, R. Tan, F. Gerdes, Z. Luo, H. Xu, J. A. Hollingsworth, C. Klinke, O. Chen, Z. Wang, *Nano Lett.* **2016**, *16*, 2792.
[45] W. van der Stam, F. T. Rabouw, S. J. W. Vonk, J. J. Geuchies, H. Ligthart, A. V. Petukhov, C. d. M. Donega, *Nano Lett.* **2016**, *16*, 2608.
[46] M. C. Weidman, D.-M. Smilgies, W. A. Tisdale, *Nat. Mater.* **2016**, 10.1038/nmat4600.
[47] A. Rossberg, T. Reich, G. Bernhard, *Anal. Bioanal. Chem.* **2003**, *376*, 631.
[48] Z. Quan, H. Xu, C. Wang, X. Wen, Y. Wang, J. Zhu, R. Li, C. J. Sheehan, Z. Wang, D. M. Smilgies, Z. Luo, J. Fang, *J. Am. Chem. Soc.* **2014**, *136*, 1352.
[49] S. Yamamuro, K. Sumiyama, *Chem. Phys. Lett.* **2006**, *418*, 166.
[50] H. Chan, A. Demortiere, L. Vukovic, P. Kral, C. Petit, *ACS Nano* **2012**, *6*, 4203.
[51] S. Disch, E. Wetterskog, R. P. Hermann, G. Salazar-Alvarez, P. Busch, T. Bruckel, L. Bergstrom, S. Kamali, *Nano Lett.* **2011**, *11*, 1651.
[52] A. I. Kitaigorodskii, *Organic Chemical Crystallography (translated from the Russian)*, Consultants Bureau, New York **1961**.
[53] M. V. Kovalenko, M. I. Bodnarchuk, R. T. Lechner, G. Hesser, F. Schaffler, W. Heiss, *J. Am. Chem. Soc.* **2007**, *129*, 6352.
[54] S. Förster, L. Apostol, W. Bras, *J. Appl. Crystallogr.* **2010**, *43*, 639.
[55] K. O. Kvashnina, A. C. Scheinost, *J. Synchrotron Radiat.* **2016**, *23*, 836.
[56] K. Momma, F. Izumi, *J. Appl. Crystallogr.* **2011**, *44*, 1272.